Supporting Information for

Earthquake Rupture Velocity and Stress-Drop Interaction in the Campi Flegrei Volcanic Caldera

Sahar Nazeri[1], Aldo Zollo[1], Titouan Muzellec[1], and Giulio Di Toro[2]

[1]Department of Physics E. Pancini, University of Naples Federico II.

[2]Department of Geosciences of the University of Padua (DG-UNIPD)

Corresponding author: Aldo Zollo (aldo.zollo@unina.it)

Contents of this file

Text S1: Data Analysis

Instrument response is removed from the raw data in the frequency domain. To remove possible baseline effects arising from low-frequency noise amplification and integration of the accelerometric or velocimetric records, a 0.1 Hz high-pass Butterworth filter is applied to the displacement signals. To proceed with the proposed method to obtain the earthquakes source parameters, the modulus of the three components' displacement waveforms for each station is used, hereinafter called eigen-waveform (Figure S1). Both P- and S-wave arrival times have been manually picked on the eigen-waveform recorded at a hypocentral distance smaller than 10 km. Although the quality of the traces has been checked whenever picking the phases, those records with low signal-to-noise ratio (SNR) are also excluded automatically from the process. The initial part of the seismic waves is used to compute the SNR using the logarithmic decibel scale and the squared amplitude ratio.

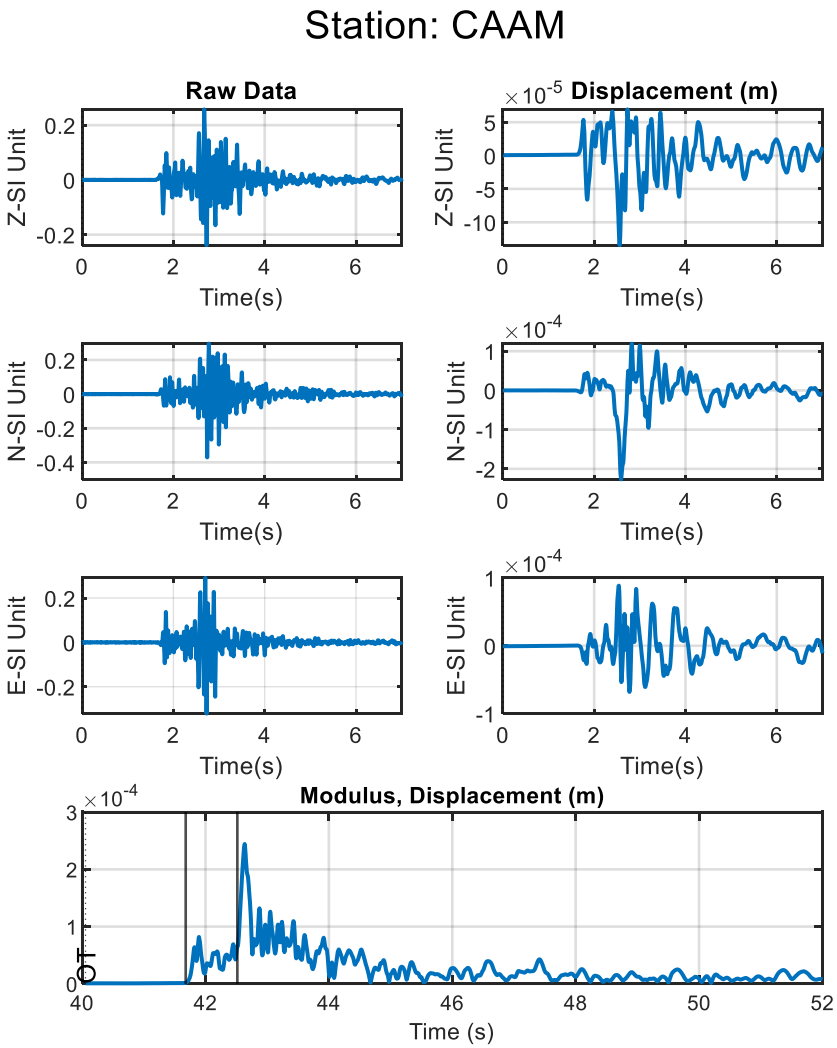

Figure S1. This figure illustrates the steps involved in generating the eigen-waveform, i.e., the "Modulus of the displacement" shown at the bottom panel. Two solid black lines show the P- and S-wave arrival times. Top panels on the left represents the raw data which for our case could be acceleration or velocity traces. Top panels on the right, show the high-passed (hp c 0.1) filtered displacement waveforms from the integration of the raw data.

Text S2: Parameter Settings for Source Characteristic Calculation

Major part of the selected events occurred at average depth of 2.5 km (Table S1), allowing us to adjust the average medium parameters accordingly for homogeneous half-space Earth' model. According to Smoothed P and S velocity model, drawn from the velocity model used by the seismic laboratory at INGV-Osservatorio Vesuviano (Calò and Tramelli, 2018), the average P-wave velocity up to this depth is about 3 km/s, resulting in 1.4 km/s for the average S-wave velocity.

The same velocity model is used to obtain the take-off angles by Taup Toolkit (Crotwell et al., 1999), needed to calculate theoretical far-field radiation patterns ($\mathcal{R}_{ph}^{\theta\varphi}$) for both seismic waves. To calculate the $\mathcal{R}_{ph}^{\theta\varphi}$, the focal mechanism solutions are required, which are obtained using the code FPFIT (Reasenberg and Oppenheimer, 1985), by considering the polarity of the first P-arrival on velocity sensors of the INGV network, only from those stations within an epicenteral distance of 8 km. To this end, an average of 11 P-polarities are available for each of the analyzed events.

Text S3: Construction of Single-Phase Source Time Function (SP-STF) with Anelastic Attenuation Correction

Figure S2a shows the initial part of the P- and S-waves of the eigen-waveforms recorded at different stations for a given earthquake, from which eigen curves of LPDT and LSDT (logarithm of the S-wave displacement amplitude vs time) are built (black solid lines in Figure S2b). For both P- and S-waves, Figure S2b shows the same waveforms whose amplitudes are corrected by hypocentral distance (grey curves) in the logarithmic scale to remove the distance-attenuation effect, whose average curves are displayed by black solid lines. In this figure, the red curve keeps the maximum amplitudes of the eigen curves in the expanding time window, used to find the best fits. Time evaluation of the curvature of the fit curve allows us to find the corner time (T_C) at which curvature tends to zero (shown with black circles in Figure S2c).

Then, couple of plateau level (P_L) and T_C is used to construct the single phase based STF (SP-STF), display in the subpanels. Indeed, corner time and plateau level are linked to the peak amplitude ($\bar{P}_d^c$) of the STF and its relevant time ($\bar{T}_H^c$) (Nazeri et al., 2019) (the superscript c is for P or S waves). Clearly, a key factor in the shape of the SP-STF is the duration, which from equations (2) and (3) (see main text, "Method" section), it relates to the rupture velocity and the observed corner time ($T_C = \bar{T}_H^c$). The attenuation-corrected peak amplitude (P_d^c) and half-duration (T_H^c), represented as $\bar{P}_{d-Q}^c$ and $\bar{T}_{H-Q}^c$, can be determined for any given Q value.

Several seismic attenuation studies based on active and passive source records, and different time and frequency domain methodologies provided the 3D images of subsoil Qp and Qs spatial variation within the shallow caldera structure (De Lorenzo et al, 2001; De Siena et al, 2010; Serlenga et al, 2016; Bianco et al, 2022; Calò and Tramelli, 2018). Since in our method an average Q-factor is assumed for the seismic attenuation correction, we selected a range of 30 to 120 for the Qp and Qs as inferred from the tomographic model of Calò and Tramelli (2018). Then the source parameters are estimated for each of the possible combination of Qp and Qs values and finally evaluated the average value of the parameter along with its uncertainty that accounts both for corner-time measurement error and the quality factor variability.

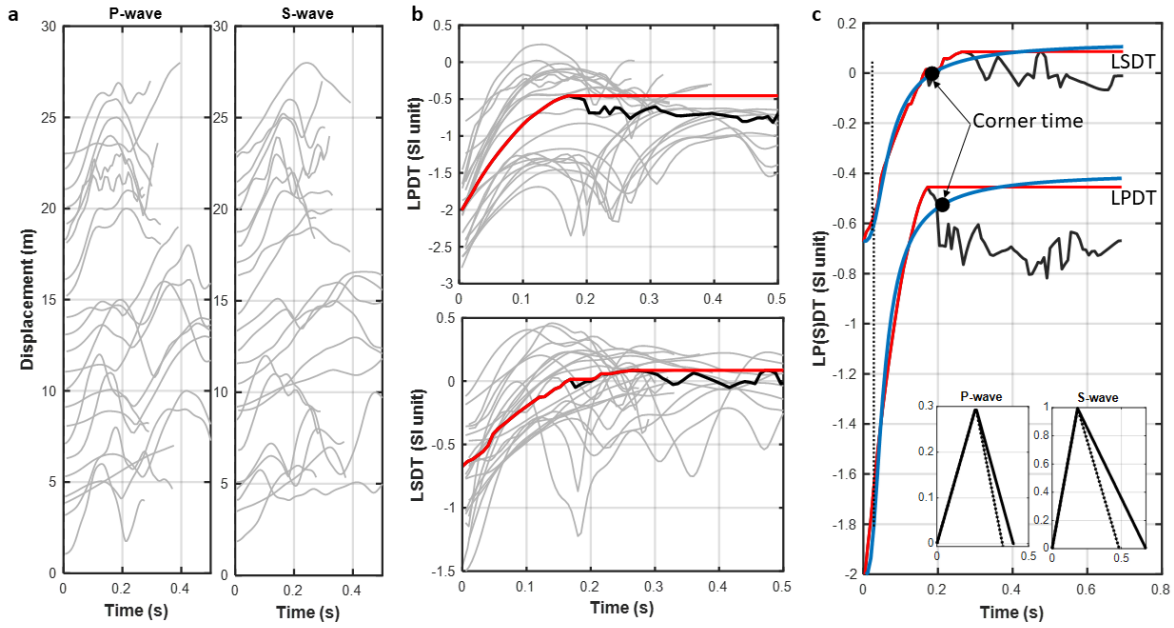

Figure S2. a. Initial part of the eigen waveforms for both P- and S-waves sorted by hypocentral distance, **b.** logarithm of the distance corrected eigen-waveforms (grey curves) and the average ones mentioned as eigen curve of LPDT and LSDT (black solid line). Red curves keep the maximum amplitudes of the eigen curves in the expanding time window, used to find the best fits. **c.** Eigen curves of the P- and S-waves and their best fit (blue curve). In the subplots, the SP-STF has been constructed using two rupture velocity values, 1. $V_r = 0.9\,V_S$, the dotted STF, and 2. V_r obtained directly from joint phases analysis (solid lines).

Text S4: Anelastic Attenuation Correction in Estimating Radiated Seismic Energy

Anelastic attenuation describes the energy loss in seismic waves due to internal friction and can be typically modeled as an exponential decay with distance (R). For anelastic attenuation, we apply the following correction relation: $E_{corrected} = E_{observed}.e^{-\alpha R}$, where α represent the attenuation coefficient, which depends on the medium and frequency. Thus, the complete formula to calculate the seismic energy corrected for attenuation at each station becomes:

$$E_{Phase,i} = const.\ R_i^2.e^{-\alpha R_i}.\int v_i^2\,(t)dt.$$

We estimate α for each phases empirically by using available data on multiple stations at various distances.

To minimize reliance on initial values of α, we worked on the relative energy content recorded at each station with respect to the energy of the closest station as a reference (R_0), where attenuation is minimal or can be approximated as negligible on this station.

Taking the logarithm of the corrected energy expression isolates α in a log-linear form, allowing us to estimate it directly. Finally, α is obtained from following log-linear relationship between the energy ratio and the distance difference $R_i - R_0$, i.e.:

$$\log\left(\frac{R_i^2.\int \dot{u}_i^2\,(t)dt}{R_0^2.\int \dot{u}_0^2\,(t)dt}\right) = -\alpha(R_i - R_0)$$

Applying this reference-based method, we found α as 0.4 and 0.3 for P- and S-wave respectively.

Text S5: Duration of the Shaking (T_d)

The duration of shaking during an earthquake, T_d, refers to the time period over which ground motion persists. This parameter can impact both the extent of structural damage and the experience of individuals during the earthquake. Following Arias (1970) and Baltay et.al., (2019), for each station T_d is calculated as an interval of 5-95% of the Arias intensity which is based on the time-domain integral of the ground acceleration defined as:

$$I_{Arias} = \frac{\pi}{2g}\int_0^{T_d} |a(t)|^2 dt$$

Figure S3 provides an example illustrating how this quantity is determined.

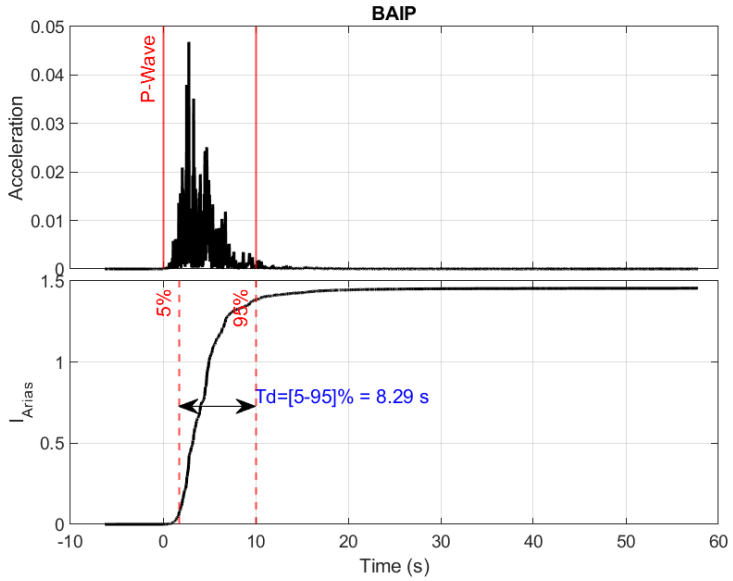

Figure S3. Modulus of the acceleration recorded at a given station and corresponding Arias intensity.

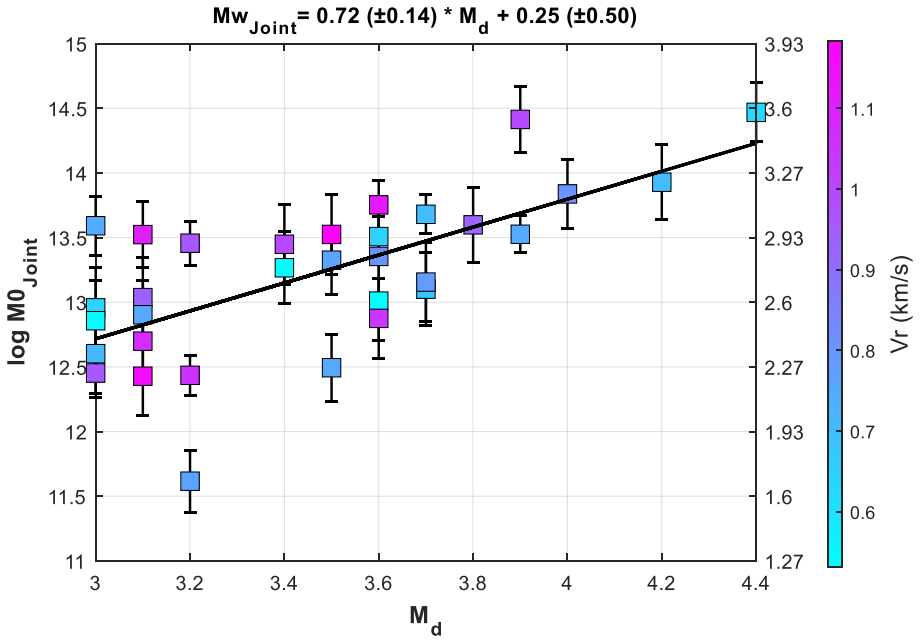

Figure S4. The seismic moment of the events calculated from joint phase analysis versus the duration magnitude.

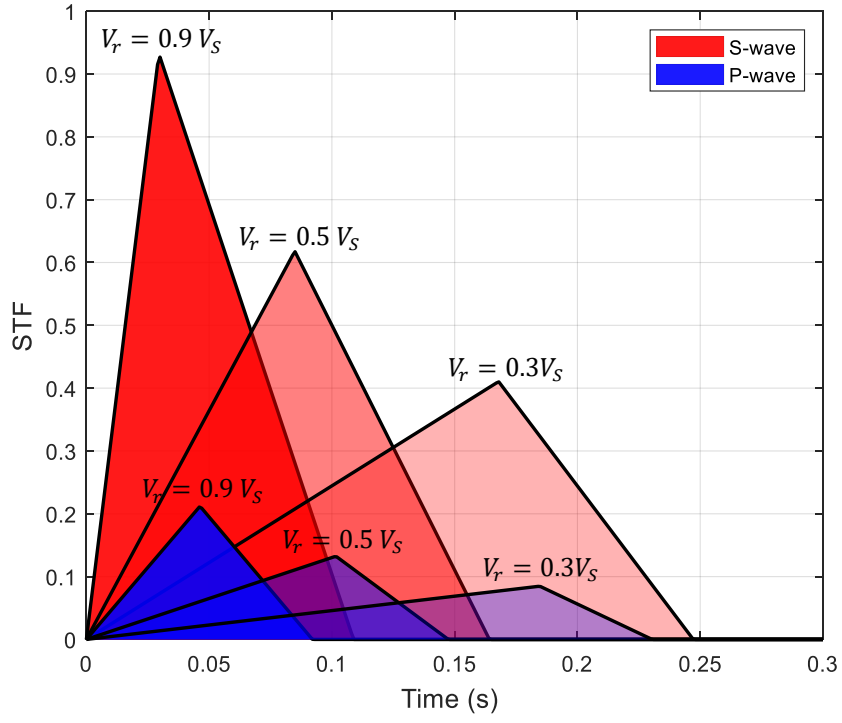

Figure S5. Representing scalene triangular STF of both P- and S-waves for a given magnitude ($M_w = 3$), stress drop value ($\Delta\sigma = 3\ MPa$), P-wave velocity ($V_P = 5\ km/s$), and S-wave velocity ($V_S = \sqrt{3}\ V_P$), assuming various rupture velocities $V_r = \alpha\ V_s$ which α varies from 0.3 (more expanded triangle) to 0.9 (more compact triangle).

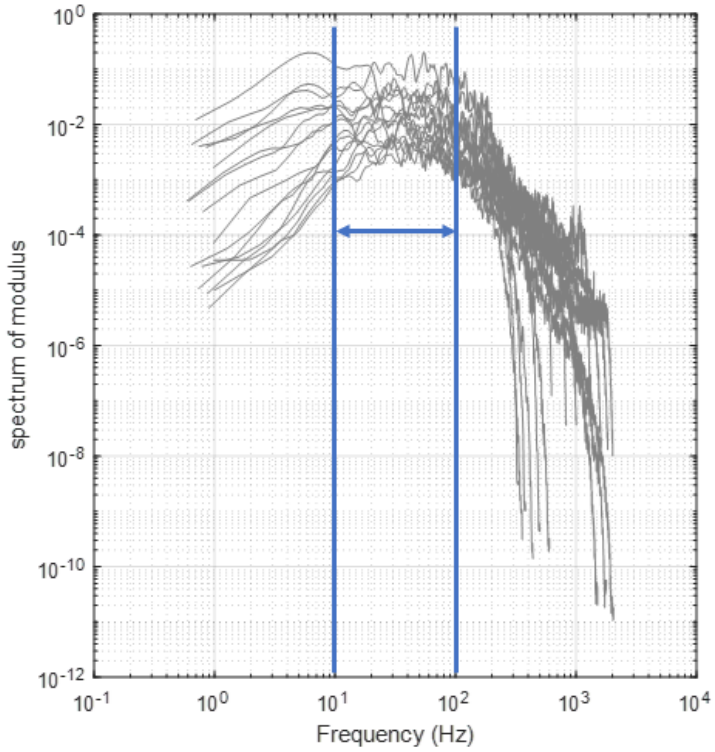

Figure S6. Spectrum of the modulus of the acceleration records for a given earthquake showing that the flat part is up to the 100 Hz.

Table S1. Dataset information, duration magnitude (INGV catalog), Location of the events is extracted from high-precision locations obtained from the work of Scotto di Uccio et al. (2024).

	Event ID	Date, Time	Latitude	Longitude	Depth (km)	Md
1	24317311	26/04/2020 02:59	40.82983	14.14850	2.54	3.1
2	30205901	16/03/2022 14:14	40.82717	14.13767	2.60	3.5
3	30350681	29/03/2022 17:45	40.82933	14.14817	2.48	3.0
4	34043501	05/02/2023 00:45	40.80650	14.11283	5.12	3.0
5	34919151	08/05/2023 02:28	40.82717	14.13750	2.60	3.4
6	35278141	11/06/2023 06:44	40.83483	14.11017	4.05	3.6
7	35871201	18/08/2023 04:09	40.82617	14.14683	2.16	3.1
8	35871351	18/08/2023 04:18	40.82900	14.14017	2.47	3.6
9	36084091	07/09/2023 17:45	40.82717	14.14100	1.71	3.8
10	36243651	22/09/2023 09:02	40.82850	14.14150	1.82	3.0
11	36288401	26/09/2023 07:10	40.80550	14.11167	3.45	3.2
12	36299321	27/09/2023 01:35	40.81717	14.15583	2.82	4.2
13	36365741	02/10/2023 20:08	40.82983	14.14850	2.46	4.0
14	36499161	16/10/2023 10:36	40.82533	14.14250	1.81	3.6
15	36951941	23/11/2023 18:41	40.82650	14.13067	2.75	3.1
16	37620831	17/02/2024 19:22	40.84050	14.11200	2.75	3.0
17	37758961	03/03/2024 09:01	40.80850	14.14917	2.57	3.4
18	38106881	04/04/2024 05:33	40.82083	14.11200	1.33	3.2
19	38206821	14/04/2024 07:44	40.82867	14.13683	2.57	3.7
20	38206811	14/04/2024 07:46	40.82900	14.13733	2.53	3.1
21	38207461	14/04/2024 08:01	40.82650	14.13367	2.22	3.0
22	38381891	27/04/2024 03:44	40.80567	14.10267	2.04	3.9
23	38525651	07/05/2024 01:47	40.82200	14.14200	1.24	3.2
24	38759411	20/05/2024 17:51	40.83933	14.13067	2.93	3.5
25	38759141	20/05/2024 18:10	40.82533	14.13783	2.66	4.4
26	38762031	20/05/2024 19:46	40.82867	14.13583	2.84	3.9
27	38762741	20/05/2024 19:55	40.82367	14.12850	2.22	3.1
28	38764921	20/05/2024 21:00	40.82133	14.12333	2.57	3.6
29	38797691	22/05/2024 06:28	40.79717	14.10783	4.26	3.60
30	39088961	08/06/2024 01:52	40.82817	14.14517	2.57	3.5
31	39089291	08/06/2024 01:52	40.83100	14.13783	1.68	3.0
32	39089101	08/06/2024 02:09	40.82783	14.14567	2.35	3.7

Table S2. Source parameters of the events from both approaches, top rows: average of single seismic phase analysis, and bottom rows: joint phase analysis.

Event ID		Vr (km/s)		logM0		Mw		a (km)		Δσ (MPa)		Slip(cm)	
1	24317311	0.93	0.06	13	0.3	2.6	0.2	154.6	47.2	1.28	1.18	1.31	0.4
2	30205901	1.18	0.02	13.5	0.3	2.9	0.2	685.5	75.6	0.05	0.02	0.19	0.02
3	30350681	0.64	0.14	13	0.3	2.6	0.2	118.1	93.1	2.4	4.29	1.87	1.47
4	34043501	0.74	0.14	13.6	0.2	3	0.2	106	53.3	14.32	4.29	3.67	1.85
5	34919151	1	0.1	13.4	0.3	2.9	0.2	422.6	109.5	0.16	0.13	0.43	0.11
6	35278141	1.12	0.05	13.8	0.2	3.1	0.1	644.3	109.5	0.09	0.05	0.17	0.03
7	35871201	1.07	0.07	12.7	0.3	2.4	0.2	510.3	109.5	0.02	0.01	0.06	0.01
8	35871351	0.81	0.14	13.4	0.3	2.8	0.2	127.4	78	4.78	4.29	4.01	2.46
9	36084091	0.93	0.11	13.6	0.3	3	0.2	340.2	109.5	0.44	0.43	1.53	0.49
10	36243651	0.53	0.13	12.9	0.3	2.5	0.2	77.3	33.8	6.81	4.29	5.07	2.22
11	36288401	0.96	0.14	13.5	0.2	2.9	0.1	237.1	106.9	0.94	1.27	0.88	0.4
12	36299321	0.7	0.14	13.9	0.3	3.2	0.2	139.6	93	13.64	4.29	10.65	7.09
13	36365741	0.8	0.14	13.8	0.3	3.2	0.2	257.7	109.5	1.76	2.24	2.98	1.27
14	36499161	0.53	0.14	13	0.3	2.6	0.2	99.3	66.3	4.56	4.29	4.35	2.9
15	36951941	0.75	0.14	12.9	0.3	2.5	0.2	214.4	107.7	0.36	0.54	0.45	0.23
16	37620831	0.95	0.1	12.5	0.2	2.2	0.1	448.4	109.5	0.01	0.01	0.04	0.01
17	37758961	0.54	0.14	13.3	0.3	2.8	0.2	195.2	109.5	1.09	1.83	1.32	0.74
18	38106881	1.06	0.08	12.4	0.2	2.2	0.1	314.4	86.7	0.04	0.03	0.16	0.04
19	38206811	1.1	0.06	13.5	0.3	2.9	0.2	953.5	109.5	0.02	0.01	0.11	0.01
20	38206821	0.68	0.14	13.1	0.3	2.7	0.2	226.8	109.5	0.47	0.69	0.67	0.32
21	38207461	0.71	0.14	12.6	0.3	2.3	0.2	240	109.5	0.13	0.17	0.23	0.11
22	38381891	0.75	0.14	13.5	0.1	3	0.1	304.1	109.5	0.52	0.56	1.35	0.49
23	38525651	0.77	0.14	11.6	0.2	1.7	0.2	101.2	61.2	0.17	0.32	0.26	0.16
24	38580291	0.7	0.09	13.7	0.1	3.1	0.1	241.5	82.3	1.49	1.52	1.13	0.39
25	38759141	0.62	0.14	14.5	0.2	3.6	0.2	190.3	109.5	18.66	4.29	17.67	10.17
26	38759411	0.76	0.14	13.3	0.3	2.8	0.2	223.8	109.5	0.82	1.21	0.97	0.48
27	38762031	1	0.1	14.4	0.3	3.5	0.2	407.2	109.5	1.68	1.36	3.82	1.03
28	38762741	1.15	0.05	12.4	0.3	2.2	0.2	381.4	88.4	0.02	0.01	0.06	0.01
29	38764921	1.04	0.08	12.9	0.3	2.5	0.2	433	109.5	0.04	0.03	0.11	0.03
30	38797691	0.65	0.14	13.5	0.2	2.9	0.1	153.7	109.5	3.88	4.29	1.57	1.12
31	39088961	0.75	0.14	12.5	0.3	2.3	0.2	148.1	97.8	0.42	0.83	0.39	0.26
32	39089101	0.79	0.14	13.2	0.3	2.7	0.2	219.9	105.8	0.59	0.85	0.95	0.46

References Supplemental Material

Calò, M., & Tramelli, A. Anatomy of the Campi Flegrei caldera using enhanced seismic tomography models. *Sci Rep*, **8(1)**, 16254 (2018).

Crotwell, H. P., Owens, T. J. & Ritsema, J. The TauP Toolkit: Flexible Seismic Travel-time and Ray-path Utilities. *Seismological Research Letters*, **70 (2)**. 154–160 (1999).

Reasenberg, P.A. & Oppenheimer, D. FPFIT, FPPLOT and FPPAGE: FORTRAN Computer Programs for Calculating and Displaying Earthquake Fault-Plane Solutions. US Geological Survey Open-File Report, 85-739, 109 p. (1985).

Nazeri, S., Colombelli, S. & Zollo, A. Fast and accurate determination of earthquake moment, rupture length and stress release for the 2016–2017 Central Italy seismic sequence. Geophys. J. Int. 217(2), 1425–1432 (2019).

Scotto di Uccio, F. S., et. al. Delineation and Fine-Scale Structure of Fault Zones Activated During the 2014–2024 Unrest at the Campi Flegrei Caldera (Southern Italy) From High-Precision Earthquake Locations. Geophys. Res. Lett. 51(12), e2023GL107680. (2024).

De Lorenzo, S., Zollo, A. & Mongelli, F. Source parameters and three-dimensional attenuation structure from the inversion of microearthquake pulse width data: QP imaging and inferences on the thermal state of Campi Flegrei caldera (southern Italy). J. Geophys. Res., 106(B8), 16,265–16,286 (2001).

De Siena, L., E. Del Pezzo, & Bianco, F. Seismic attenuation imaging of Campi Flegrei: Evidence of gas reservoirs, hydrothermal basins, and feeding systems. J. Geophys. Res. 115, B09312 (2010).

Serlenga, V. et. al. A three-dimensional QP imaging of the shallowest subsurface of Campi Flegrei offshore caldera, southern Italy. Geophys. Res. Lett. 43(21), 11,209-11,218. (2016).

Bianco, F. et al. Seismic and Gravity Structure of the Campi Flegrei Caldera, Italy. In: Orsi, G., D'Antonio, M., Civetta, L. (eds) Campi Flegrei. Active Volcanoes of the World. (Springer, Berlin, Heidelberg, 2022).

Calò, M., & Tramelli, A. Anatomy of the Campi Flegrei caldera using enhanced seismic tomography models. Sci Rep, 8(1), 16254 (2018).